HHS Public Access

Author manuscript

IEEE Access. Author manuscript; available in PMC 2024 December 26.

Published in final edited form as:

IEEE Access. 2024 ; 12: 164315–164324. doi:10.1109/access.2024.3491592.

Volumetric Patch-Based Super-Resolution Reconstruction of Hyperpolarized ^{13}C Cardiac MRI

SUNG-HAN LIN[1], **JUNJIE MA**[2], **JAE MO PARK**[1] **[Member, IEEE]**

[1]University of Texas Southwestern Medical Center, Dallas, TX 75390, USA

[2]GE Healthcare, Jersey City, NJ 07302, USA

Abstract

The achievable spatial resolution of ^{13}C metabolic images acquired with hyperpolarized ^{13}C-pyruvate is worse than ^{1}H images typically by an order of magnitude due to the rapidly decaying hyperpolarized signals and the low gyromagnetic ratio of ^{13}C. This study is to develop and characterize a volumetric patch-based super-resolution reconstruction algorithm that enhances spatial resolution ^{13}C cardiac MRI by utilizing structural information from ^{1}H MRI. The reconstruction procedure comprises anatomical segmentation from high-resolution ^{1}H MRI, calculation of a patch-based weight matrix, and iterative reconstruction of high-resolution multi-slice ^{13}C MRI. The method was tested with a multi-compartmental digital phantom for optimizing the patch size and an anthropomorphic cardiac MR phantom for validating the performance. Finally, the method was applied to human cardiac ^{13}C images, acquired with an injection of hyperpolarized [1-^{13}C]pyruvate. The phantom studies demonstrated that high-resolution multi-slice ^{13}C images, reconstructed from a single-slice low-resolution input ^{13}C image, retained the signal intensity range. The reconstruction accuracy was asymptotically improved as the patch size increased whereas intra-segmental spatial fluctuations were preserved better with smaller patches. However, a structurally non-identified tissue region was not restored regardless of the patch size. The cardiac MR phantom and the human cardiac images demonstrated improved spatial resolutions in the reconstructed images ($10 \times 10 \times 30$ mm^3/voxel to $2 \times 2 \times 5$ mm^3/voxel). The volumetric patch-based super-resolution method reconstructs multi-slice high-resolution of ^{13}C images, enhancing the cardiac structure, while preserving the quantitative accuracy. The proposed method is applicable to other multi-modal images that suffer from limited spatial resolution.

Keywords

Cardiovascular system; reconstruction algorithm; image resolution; magnetic resonance imaging; metabolism

Corresponding author: Jae Mo Park (jaemo.park@utsouthwestern.edu).

This work involved human subjects or animals in its research. Approval of all ethical and experimental procedures and protocols was granted by UT Southwestern IRB (Institutional Review Board) under Application No. STU-2018-0227.

I. INTRODUCTION

CARBON-13 (^{13}C) MRI with hyperpolarized (HP) [1-^{13}C]pyruvate captures key enzymatic steps of carbohydrate metabolism such as lactate fermentation, reductive amination of pyruvate, and pyruvate oxidation in the heart. Due to the unique capability of assessing the metabolic fate of pyruvate in the myocardium and the advantage of using the stable isotope without ionizing radiation, the technique has been quickly translated to cardiac metabolic imaging in humans [1], [2], [3], [4]. However, the rapidly decaying HP signals and the time-varying nature of metabolic information require an instant acquisition of ^{13}C data, yet the quarter-size gyromagnetic ratio of ^{13}C compared to ^{1}H slows down the data collection, limiting the achievable spatial resolution of HP ^{13}C images. Leveraging the sampling balance between k-space and spectral domains escalates the technical challenges due to mechanical and metabolic oscillations associated with the cardiac cycle. The existence of high-resolution structural ^{1}H images may offer the opportunity to overcome the limited spatial resolution in metabolic ^{13}C images without altering the acquisition scheme.

The currently dominant acquisition method for cardiac HP ^{13}C MRI is a metabolite-interleaved spiral imaging with spectrally-spatially selective RF pulses, taking advantage of the large chemical shift dispersion between the HP metabolites [1], [5], [6], [7], [8], [9]. The achievable voxel size, however, remains in the order of centimeters, which is much larger than conventional ^{1}H cardiac images. While the discrepancy in spatial resolution between anatomical (^{1}H) and metabolic (^{13}C) images hampers precise localization and metabolic assessment of the regions of interest, the high-resolution ^{1}H MRI can provide structural guidance to augment the spatial resolution of ^{13}C images. Recent studies have developed reconstruction methods that exploit ^{1}H MRI for enhancing the spatial resolution of HP ^{13}C images in the brain [10], [11], [12], [13]. However, the complex metabolic distinction between cerebral compartments in HP metabolite maps obscures the selection of the structural guideline and its validation. Moreover, the previous methods were limited to in-plane reconstruction [10], [13], focused on preclinical kinetic analysis [11], or directly regularized by structural images [12].

The compartmental distribution of HP signals is less ambiguous in the heart. For instance, [^{13}C]bicarbonate and [1-^{13}C]pyruvate are predominantly from the myocardium and the ventricle, respectively, and [1-^{13}C]lactate are typically from both tissue compartments [1]. In this study, we developed a 3D ^{13}C super-resolution method that uses multi-slice ^{1}H patches for volumetric anatomical references and investigated its performance with cardiac phantoms and *in vivo* human cardiac MRI. The current method extends the previously presented two-dimensional patch-based super-resolution (PBSR) method [13] to a volumetric reconstruction by introducing additional dimension along the through-plane direction.

II. METHODS

A. VOLUMETRIC PBSR RECONSTRUCTION

The proposed method utilizes multi-slice cardiac ^{1}HMRI that contains high-resolution anatomical information for reconstructing a low-resolution single-slice metabolic ^{13}C MRI

into multi-slice images with enhanced in-plane spatial resolutions. The reconstruction procedure comprises three steps as illustrated in Fig. 1.

First, multi-slice, high-resolution structural ^{1}H MR images ($I_{HR}^{H,M} \in \mathbb{R}^{N_{HR,x} \times N_{HR,y} \times N_{sl}}$) are down-sampled to a targeted spatial resolution ($I_{SR}^{H,M} \in \mathbb{R}^{N_{SR,x} \times N_{SR,y} \times N_{sl}}$) and segmented to create probability maps ($P_{SR}^{H,M} \in \mathbb{R}^{N_{SR,x} \times N_{SR,y} \times N_{sl} \times N_{CP}}$), where the subscripted HR, SR, sl, and CP stands for highresolution, super-resolution, slice, and compartment, respectively. The superscripted H and M are for ^{1}H and multi-slice, respectively. In parallel, single-slice, low-resolution ^{13}C metabolic images ($I_{LR}^{C,S} \in \mathbb{R}^{N_{LR,x} \times N_{LR,y} \times N_{MT}}$) are up-sampled to the targeted super-resolution ($I_{SR}^{C,S} \in \mathbb{R}^{N_{SR,x} \times N_{SR,y} \times N_{MT}}$), where LR and MT stands for low-resolution and metabolites, respectively. The superscripted C and S are for ^{13}C and single-slice, respectively. As demonstrated in our previous 2D PBSR [13], having probability maps that aligned to ^{13}C images is required for optimally enhancing spatial resolution although inaccurate segmentation does not compromise quantification accuracy or the intra-compartment signal inhomogeneity. Thus, if needed, the processed ^{13}C images ($I_{SR}^{C,S}$) are manually aligned by repositioning the prepared ^{1}H images ($I_{SR}^{H,M}$) and probability maps ($P_{SR}^{H,M}$) until they are correctly overlaid on the ^{13}C images.

Second, a patch-based weight matrix (PBWM) is calculated from the aligned ^{1}H images ($I_{SR,a}^{H,M}$, $P_{SR,a}^{H,M}$) for a designated patch size using (1).

$$w(\mathbf{x}_i, \mathbf{x}_j) = \frac{1}{Z_i \cdot K} \sum_{c=1}^{N_{CP}} P_{i,c} \cdot P_{j,c} \cdot e^{-\frac{\| \hat{N}_i - \widehat{N}_j \|^2}{2\sigma_i^2}} \tag{1}$$

The weight $w(\mathbf{x}_i, \mathbf{x}_j)$ quantifies the contribution of neighborhood pixel $\mathbf{x}_j$ in the reconstruction of $\mathbf{x}_i$. $\hat{N}_i$ and $\hat{N}_j$ are the intensity vectors of the neighborhood voxels, V_i and V_j, around voxels i and j. σ_i represents the standard deviation of the neighborhood voxels in $\hat{N}_i$. $P_{i,c}$ and $P_{j,c}$ are the probabilities that the voxels i and j belong to compartment c. Z_i is a normalization factor that is defined in (2).

$$Z_i = \sum_{j \in V_i} w(x_i, x_j) \tag{2}$$

Since the weight function is meticulously crafted through the amalgamation of two principal components [14], down-sampled ^{1}H structural images and segmentation maps that are tailored to conform to the target reconstruction dimension, it can define the contribution of neighborhood voxels.

Third, multi-slice ^{13}C MRI are calculated ($I_{SR(n)}^{C,M} \in \mathbb{R}^{N_{SR,x} \times N_{SR,y} \times N_{sl} \times N_{MT}}$), initially by replicating the aligned single-slice ^{13}C MRI ($I_{SR,a}^{C,S}$), then by iteratively updating them using

(3) until the maximum error between iterations becomes below a predetermined threshold (θ). n indicates the number of iterations. The iterative process redistributes ^{13}C signals from the initial up-sampled, single-slice to multi-slices under the guidance of the defined weight function. To prevent instances of never reaching the threshold, the number of expected iterations is estimated, based on the first ten iterations and the threshold, by a nonlinear least square approach. In this study, the threshold and the maximum number of iterations were empirically set to 10^{-8} and 1000, respectively, to safely determine that the reconstructed images are saturated. The MATLAB source code and exemplary data are available at: https://github.com/Sung-hanLin/3DPatchSupRes

$$I_{SR(n)}^{C,M}(x_i) = \sum_{j \in V_i} w(x_i, x_j) \cdot I_{SR(n-1)}^{C,M}(x_j) \tag{3}$$

B. ^{1}H/^{13}C DIGITAL PHANTOMS FOR SIMULATIONS

A numerical 3D digital phantom, which depicts a cross-sectional view of the left ventricle on short-axis plane in the heart, was generated by modifying a 3D Shepp-Logan phantom using MATLAB (MathWorks, Natick, MA, USA). The solid oval and the hollow oval compartments in the digital phantom simulate ventricular HP [1-^{13}C]pyruvate and myocardial HP [^{13}C]bicarbonate signals, respectively (Fig. 2). Three major compartments are generated, including the left ventricle, the myocardium, and the surrounding area in the chest. Both ^{1}H (structural) and ^{13}C (metabolic) images were created using the digital phantom image. Ten slices of structural images (matrix size = 512 × 512 × 10) were generated for ^{1}H images. In addition, a lesion strip was created to mimic a small-scale ischemic region in the myocardium. While ischemia is most common in the left ventricular wall, it can occur in any tissue area in the left ventricle [15]. For this simulation, we created the lesion within the 6th slice near the inner boundary of the myocardium with relatively higher lactate signals.

A separate set of the metabolite maps (matrix size = 192× 192 × 10) was generated as the high-resolution ground truth of total ^{13}C images. Three segmented compartmental maps were generated for the myocardium, the ventricle, and the rest tissue region. The ischemic lesion was not considered as a separate probability map since the primary purpose of the lesion was to test whether the PBSR can reconstruct it without having the lesion-specific probability map guidance. The results were later compared to those reconstructed with a dedicated compartment map. Considering that [1-^{13}C]pyruvate and [^{13}C]bicarbonate and are primarily from the ventricles and the myocardium, respectively [1], [3], spatial distribution of metabolite intensities were assigned differently for bicarbonate (ventricle: myocardium: ischemia = 0.1: 1.1: 0), pyruvate (1: 0.11: 0) and lactate (1: 1.1: 1.5). Note that these relative metabolite distributions are for simulation only and do not represent actual *in vivo* cases. The ischemic lesion was set to have no bicarbonate and pyruvate signals but elevated lactate signal. The ground truth metabolic images are shown in Fig. 2c. Single-slice, low-resolution ^{13}C metabolite maps (Fig. 2d), used as input images for simulations, were generated by adding up the multi-slice ground truth images of each metabolite and down-sampling (matrix size = 12 × 12 × 1).

The PBSR-reconstructed images and their corresponding ground truth were compared slice-wise by measuring mean square errors (MSE) and structural similarity index measure (SSIM). SSIM was calculated using (4) [16], where μ_x, μ_y, σ_x, σ_y, σ_{xy} indicate local means, standard deviations and covariance for input images, I_x and I_y. The hyperparameters, $\{C_1, C_2, C_3\}$, were set to $(0.01L)^2, (0.03L)^2, (0.03L)^2/2\}$, where L is the dynamic range of the images, and α, $\beta, \gamma = 1$.

$$SSIM(I_x, I_y) = \left(\frac{2\mu_x\mu_y + C_1}{\mu_x^2 + \mu_y^2 + C_1}\right)^{\alpha} \cdot \left(\frac{2\sigma_x\sigma_y + C_2}{\sigma_x^2 + \sigma_y^2 + C_2}\right)^{\beta} \cdot \left(\frac{\sigma_{xy} + C_3}{\sigma_x\sigma_y + C_3}\right)^{\gamma} \quad (4)$$

C. CARDIAC MR PHANTOM FOR PERFORMANCEVALIDATION

All MR images were acquired from a clinical 3T wide-bore (diameter $\varnothing = 70$ cm) MRI scanner (750W Discovery, GE Healthcare, Waukesha, WI, USA). The body coil was used for ^{1}H imaging and a two-loop ^{13}C transmit/receive coil was used for ^{13}C imaging $\varnothing = 20$ cm, PulseTeq Limited, Chobham, Surrey, UK). An anthropomorphic torso phantom (Data Spectrum, Hillsborough, NC) with a heart insert, filled with gadolinium-doped 0.4-M [^{13}C]bicarbonate, was scanned. The ^{1}H/^{13}C-integrated imaging protocol included a 2D ^{1}H multi-slice T_1-weighted gradient echo (TE = 1.712 ms, TR = 4.442 ms, field-of-view [FOV] = 400 × 400 mm^2, matrix size = 512 × 512 × 10, spatial resolution = 0.78×0.78 × 3 mm^3/pixel) and a 2D ^{13}C single-slice metabolite-interleaved multi-echo spiral imaging that excited a single metabolite using a spectral-spatial RF pulse at a time (TE = 18.42 ms, TR = 5000 ms, FOV = 400 × 400 mm^2, matrix size = 40 × 40 × 1, spatial resolution = 10 × 10 × 30 mm^3/pixel, 4 echoes) along the short-axis view [7].

D. IN VIVO HUMAN CARDIAC IMAGING PROTOCOL

A set of *in vivo* cardiac images were acquired from a healthy volunteer (Female, 50 years old) using the identical experimental setup. One loop of the dual-loop ^{13}C RF coil was positioned on the anterior chest, and the other was below the subject's scapula. All images were acquired with ECG gating. The subject received two consecutive injections of 250-mM HP [1-^{13}C]pyruvate solution with a 30-minute interval for ^{13}C imaging along short-axis and long-axis views. The polarization procedure, injection parameters, and ^{13}C imaging are identical to our previous study [7]. Briefly, the images of HP [^{13}C]bicarbonate, [1-^{13}C]lactate, and [1-^{13}C]pyruvate were acquired in an interleaved manner every two R-R intervals using the metabolite-selective multi-echo spiral imaging sequence (FOV = 400 × 400 mm^2, matrix size = 40 × 40 × 1, spatial resolution = 10 × 10 × 30 mm^3 /pixel, #echo = 4) [7]. ^{1}H images were acquired using T_1-weighted FIESTA (FOV = 400×400 mm^2, matrix size = 256×256 × 6, spatial resolution = 1.56 × 1.56 × 5 mm^3/pixel). The imaging protocol was approved by the local Institutional Review Board (IRB#: STU-2018–0227).

E. IMAGE RECONSTRUCTION AND EVALUATION METRICS

The volumetric PBSR reconstruction was applied to the single-slice metabolic ^{13}C images of the digital phantom, the MR phantom, and the *in vivo* cardiac images to generate multi-slice higher-resolution images. Various sizes of patches from 3 × 3× 3 to 25 × 25× 9 of neighborhood voxels with an isotropic size increment of two were generated from the structural ^{1}H images and applied to the digital phantom to test reconstruction accuracy and computation loadings. To prevent the weight matrix from being dominated by zeros along the slice dimension, the maximum patch size along this dimension was limited to the number of slices. Similarly, 3 × 3× 3 to 15 × 15× 9 and 3 × 3× 3 to 9 × 9× 5 patches were tested for the torso phantom and the *in vivo* cardiac images, respectively. During the iterative reconstruction step, a predicted total iteration number was estimated by a power curve fitting function of the mean correction errors from the first ten iterations.

The reconstructed image was quantitatively assessed with the averaged signal intensity and the signal-to-noise ratio (SNR), defined by the National Manufacturers Electrical Association (NEMA). The ratio of the mean signal intensity (S) from the main object to the standard deviation of the random noise (N) from four corners of the image, was multiplied by 0.655, the Rayleigh distribution correction factor, to calculate the SNR. The ventricular and myocardial signals were evaluated separately. For the digital phantoms, the similarity between the reconstructed images and corresponding ground truth was assessed with MSE and SSIM. In addition to the global assessment, the 6^{th} slice that contains the ischemic lesion was separately evaluated for MSE and SSIM to highlight the performance of the PBSR reconstruction over the unguided reconstruction. The entropy of low-resolution ^{13}C images was calculated to assess the randomness and complexity of each image.

We compared the performance of the PBSR-reconstructed images with the method developed by Ehrhardt, et al. [12], which enhances the spatial resolution of HP ^{13}C images using a directional total variation regularizer. For the 3D directional total variation reconstruction (3D-dTV), we used the software and parameters provided by the authors [12] (https://github.com/mehrhardt/Enhancing_hMRI.git). The torso phantom and *in vivo* HP ^{13}C cardiac images were used for the comparison. Since the intensity of images reconstructed by the 3D-dTV was scaled, both PBSR-reconstructed and 3D-dTV-reconstructed images were normalized to have a maximum signal intensity of 1 before creating a difference map.

III. RESULTS

The performance of the PBSR reconstruction evaluated using the cardiac $^{1}H/^{13}C$ digital phantom is shown in Fig. 3. Overall, the quantitation accuracy of the reconstructed images increased with the patch size (Fig. 3a). The averaged reconstructed signal intensities were lower than the ground truth by 11 – 19 % when a 3 × 3× 3 patch was used, except for the myocardial pyruvate. The amount of the signal drop was smaller for a metabolite map with a higher entropy. The entropy of the input images is summarized in Table 1. The signal intensities were gradually restored with larger patches until plateaued with a 15 × 15 × 9 patch. A similar pattern was observed for the SNR (Fig. 3b) as the noise level in the reconstructed images was comparable across all metabolites and patch sizes. For all patches,

SNR of the reconstructed images was improved by more than 50-fold as compared to the ground truth. The MSE (Fig. 3c) and SSIM (Fig. 3d) were also asymptotically improved as the patch size increased, then stabilized. Notably, [^{13}C]bicarbonate achieved a saturation level with a smaller patch (e.g., 9 × 9 × 9) and [1-^{13}C]pyruvate had the lowest SSIM as compared to the other metabolites. For each metabolite, a larger MSE and a lower SSIM were measured from the lesion-inserted slice than those from the entire volume. Edge slices were more susceptible to errors, associated with a patch, than the central slices. In particular, unallocated signals appeared in the first slice for all ^{13}C metabolites when a 9×9 × 9 or smaller patch was used. The complete set of reconstructed digital phantom images using each patch size is in Supporting Information (Fig. S1).

The ischemic lesion was not restored in all reconstructed metabolic images since it was not included in the probability maps. Cross-sectional intensity profiles along horizontal and vertical reference lines drawn across the lesion with selected patch sizes are highlighted in Fig. 4. The corresponding metabolite maps are included in the Supporting Information (Fig. S2). The PBSR-reconstructed bicarbonate and pyruvate images did not present any signal change in the lesion regardless of the patch sizes. In contrast, lactate map reconstructed using a 3 × 3 × 3 patch showed an elevated signal over the lesion. In general, intra-segmental signal variations were retained better with smaller patches (e.g., 3rd, 6th, and 9th slices). Cross-sectional signal intensity profiles of all slices are available in the Supporting Information (Fig. S3 – S5). The MSEs were comparable between different patch sizes, but relatively higher MSEs were consistently measured in the middle slices (Fig. S6). When a separate probability map was defined for the ischemic lesion, the lesion was correctly restored in the PBSR-reconstructed images, Fig. 5.

The patch size for reconstructing the anthropomorphic torso phantom and *in vivo* human heart images was set to 7 × 7 × 7 and 7 × 7 × 5, respectively, considering the simulation result that showed nearly saturated performance with a 7 × 7 × 7 patch as well as computational complexity and the slice thickness ratio between ^{13}C and ^{1}H. The reduced patch size along the slice direction for the *in vivo* images is due to fewer proton image slices within the ^{13}C slice. Fig. 6 shows the anthropomorphic torso phantom results. Multi-slice ^{13}C images were reconstructed by the PBSR method with the matching signal distribution with the anatomical ^{1}H images, creating a series of concentric rings with decreasing diameter towards the apex. The signal intensities of the acquired single slice ^{13}C image and the projected sum of the reconstructed images were comparable. Structural similarity between the single-slice image and the stacked-up reconstructed images was strong (SSIM=0.9943). The susceptibility artifact found at the air-liquid interface on the right side of the circular shape of the heart insertion was preserved in the reconstruction images. Approximately 60% of the maximum signal intensity was present at the central cavity in the low-resolution input due to partial volume effects and contribution from the apical signals, and this contrast was maintained. The 3D-dTV-reconstructed bicarbonate images had higher SNRs (Fig. S7). However, while only the myocardial compartment was supposed to show ^{13}C signals, the 3D-dTV also reconstructed ^{13}C signals in the plastic wall of the phantom as well as the ventricle compartment, where no ^{13}C signal was present (Fig. 6g).

The PBSR-reconstructed HP ^{13}C images of the human heart in the short-axis and the long-axis planes are shown in Fig. 7 and Fig. 8, respectively. Three compartmental maps, manually segmented from the anatomical images, for the myocardium, ventricle, and the rest tissue region are shown in the second row of each figure. Overall, the ^{13}C images were reconstructed to follow the structural shape and to redistribute the signal intensity from the low-resolution single slice into six slices. The signal intensity range of the projected sum of the reconstructed images was maintained, as summarized in Table 2. Overall, the volumetric PBSR algorithm sharpened the ^{13}C images, enhancing the cardiac structure and the boundary and reconstructed the through-plane signal distribution. Note that the reconstructed multi-slice images are overlaid on top of the corresponding anatomical ^{1}H images. Non-overlaid images are included in the Supporting Information (Fig. S8 and Fig. S9). Artifact lines, marked as white arrowheads in the supporting figures, were introduced on the right-side edges of the reconstructed images due to the insufficient FOV in the structural image. Unlike the phantom study where perfect segments can be identified, the SNR did not improve in the stacked-up images (Table S1) and the peak SNR improved only by 25.1 ± 14.5 % as compared to the input (Table S2). For comparison, the 3D-dTV method was also applied to the *in vivo* ^{13}C images. Artifacts appeared in the regions with a higher signal contrast to their neighborhoods in the reference ^{1}H structural images (arrowheads in Fig. S10 and Fig. S11), and the reconstructed ^{13}C signals showed a partial outline of the chest outside of the heart, which might result from the reference structural images. In addition, the reconstructed signals in the long-axis view showed signal bleeding into neighboring compartments.

IV. DISCUSSION

Several reconstruction methods have been proposed to overcome the inherently low spatial resolution of non-proton MR spectrum images by incorporating guidance from high-resolution structural images. One type of approach combines anatomical images with MR spectrum images in the k-space domain to enhance the high-frequency component and establish the boundary using discrete Fourier transform [17], [18]. Another major type of approach exclusively operates in the image domain, utilizing structural images as edge and contrast information sources [19], [20], [21]. Methods for HP images were developed using the second approach and primarily focused on the brain [10], [12], [13].

Our PBSR method is also an extension of the second approach as all the procedures are performed in the image domain and utilize structural images as the source of edge and contrast information. The PBSR method was originally developed for image denoising by employing non-local averages of neighborhood pixels that retain the signal continuity and changes between pixels in the reconstructed images [14], [22]. Indeed, our results showed that the volumetric PBSR reconstruction improves through-plane spatial resolution and SNR. The ^{13}C images reconstructed from the torso phantom showed a decreasing size of the bicarbonate radius towards the apex of the heart in short-axis view, reflecting the anatomical changes.

In this study, we demonstrated that the proposed 3D PBSR method outperformed the 3D-dTV in reconstructing cardiac images in terms of 1) preserving the signal intensities of

the raw ^{13}C images 2) without being dominated by the structural information and creating artifacts. The major difference between the methods is that the 3D-dTV heavily relies on the structural ^{1}H image while both utilize the ^{1}H segmentation map to set up the ^{13}C signal distribution boundary.

A. SELECTION CRITERIA OF THE PATCH SIZE

The PBWM regulates how ^{13}C signals in a single slice are distributed to multiple slices. Both the digital and torso phantoms showed that the proposed PBSR algorithm is sensitive to the patch size. As the amount of anatomical information increases with the patch size, a larger patch led structurally more accurate guidance in the iterative reconstruction procedure. This observation reflects that the PBSR algorithm considers the signal continuity and redundancy between two neighboring pixels and performs better by averaging a sufficient number of pixels [23]. Along the same reference line, some signals appeared in the wrong compartments when a small patch was used (Fig. S1), likely due to the insufficient information transferred from the patch to the super-resolution image. In contrast, small patches tended to be more sensitive to intra-compartmental signal fluctuations (Fig. 4). Collectively, the results suggest that a larger patch would provide a more accurate reconstruction in signal intensity but flatten the details, being less sensitive to the signal fluctuations between pixels (Fig. S3 – S5).

The accuracy of reconstructed images asymptotically improves and gets ultimately saturated as the patch size increased. However, as the patch size becomes larger, the computational complexity keeps rising. In our study, the 25 × 25 × 9 patch weighting matrix occupied approximately 64 GB of memory and 4.3 hours of parallel computing for a 6-core workstation. The computation of the weight matrix constitutes the bulk of the processing load, increasing exponentially with the growth of the patch size. The PBWM size is proportional to both the reconstructed image size and the patch size. Every time the patch size increases by two along each dimension, the PBWM grows by a factor of R, which is given in (5).

$$R = \frac{(N_{SR,x}+2)\cdot(N_{SR,y}+2)\cdot(N_{sl}+2)\cdot(P_x\cdot P_y\cdot P_z)}{N_{SR,x}\cdot N_{SR,y}\cdot N_{sl}\cdot P_x\cdot P_y\cdot P_z} \tag{5}$$

Thus, seeking the minimum patch size requirement to the saturated level of reconstruction image quality is critical for computational efficiency. Two factors can be considered for determining the patch size to use: the input image complexity (i.e., entropy) and the spatial enhancement ratio (N_{SR}/N_{LR}). An image with high complexity requires to gather spatial details around each voxel using a large patch. On the other hand, the enhancement ratio does not only require a larger patch to gather more neighborhood information [24] but also affect the computational complexity of the reconstructed outcome. In our study, the digital phantom required a 15 × 15 × 9 patch for the enhancement ratio of 16 (192/12) while a 7 × 7 × 7 patch was sufficient for the torso phantom and human cardiac images with the ratio of 4.8 (192/40). The small patch size (7 × 7 × 7) for the MR studies is also

likely attributed to the structural simplicity (cylindrical shape) and its consistency along the through-plane dimension. For patient populations with more heterogenous compartments and lesions, a larger patch size may be necessary. The practical selection of patch size should be the smallest one beyond which further increases lead to negligible improvements in image quality metrics, considering the exponentially increasing computational load and the saturating reconstruction performance with larger patch sizes.

B. IMPORTANCE OF PRECISE PROBABILITY MAPS AND FEASIBILITY OF RECONSTRUCTING HIGH FREQUENCY COMPONENTS

The probability map of each tissue region needs to be precisely identified in high-resolution images for ideal performance. As demonstrated in our simulation results, the ischemic lesion could not be reconstructed properly without having a dedicated probability map. When the lesion was properly segmented, the reconstructed [1-^{13}C]lactate image correctly displayed the lesion (Fig. 5). The lesion was also revealed in [^{13}C]bicarbonate image. Moreover, considering that the narrow lesion represents a relatively high spatial frequency component, the results suggest that high frequency features can be reconstructed by incorporating accurate segmentation maps.

Inaccurate image reconstruction and the presence of artifacts can lead to misinterpretation of the image and result in critical clinical errors, impacting diagnostic accuracies and treatment planning. Incorporating with additional input source for image reconstruction, therefore, requires careful validation to ensure quantitative accuracy and to determine whether it introduces artifacts. Few cases of inaccurate segmentation from high-resolution ^{1}H MRI were previously investigated with the 2D PBSR method [13]. Consistently with the previous study, we did not observe any signal loss in reconstructed ^{13}C images for pixels included in the segmentation map (Fig. S3–S5). Moreover, the presence of the lesion strip in anatomical images did not result in false-positive issues in ^{13}C images in this study. However, we noticed signal fluctuations at the edges of lesions when the patch size was small.

C. POTENTIAL BENEFITS OF PBSR IN HP ^{13}C CARDIAC MRI

Unlike HP [1-^{13}C]pyruvate that is mainly detected in the cardiac chambers, HP [^{13}C]bicarbonate is produced predominantly in the myocardium where HP [1-^{13}C]pyruvate is metabolized to acetyl-CoA via a mitochondrial enzyme, PDH. Several studies reported that the abnormal distribution of HP [^{13}C]bicarbonate could reflect altered pyruvate oxidation, a key pathophysiological biomarker of cardiomyopathies [3], [25], [26]. Although production of HP [1-^{13}C]lactate is less tissue-specific, elevated lactate level in the myocardium is also correlated to myocarditis [27] and accumulation of [1-^{13}C]lactate would be the early sign of cardiac ischemia [28]. The enhanced spatial resolution along the through-plane dimension is expected to improve spatial localization of metabolic aberration and, thus, the clinical diagnosis of cardiomyopathy. Moreover, although not intensively investigated in this study, PBSR-reconstructed images improved the SNR over the ground truths, implying a denoising feature of the method [22].

D. LIMITATIONS AND FUTURE IMPROVEMENT

Several limitations are identified in the study. First, misregistration between ^{1}H and ^{13}C MRI can result in incorrect reconstruction since the proper segmentation is critical in the PBSR reconstruction. Considering that cardiac images are particularly prone to spatial mismatch due to the motion, changes of the cardiac rate between ^{1}H cine and ^{13}C MRI may result in artifacts. For instance, although the *in vivo* cardiac ^{13}C MRI was targeted at end-diastole, the trigger delay pre-calculated from a separate ^{1}H cine MRI might have missed the end-diastole. As demonstrated in the digital phantom simulation and our previous study [13], metabolically outstanding lesions could not be fully reconstructed without the corresponding segmentation maps, highlighting the dependency of the PBSR reconstruction on accurate segmentation and the importance of correct alignment between ^{1}H and ^{13}C images. The PBSR's sensitivity to the spatial misalignment between the structural and metabolic images may be useful for future investigation of the heart phase correction [29]. The insufficient improvement in SNR observed from *in vivo* data might also be due to this. Second, the selection process of patch size can be improved. As the optimal patch size for each case varies, depending on the image complexity and size, the optimal patch size needs to be determined during the reconstruction pipeline. Third, the ^{13}C slice profile was assumed to be ideal. Incorporating actual, non-ideal slice profile in the reconstruction may improve the reconstruction results, reducing the contribution to the signal further away from the slice center. Finally, the segmentation approach from structural guidance might not be sufficient for achieving the optimal performance of PBSR reconstruction of HP ^{13}C MRI. Additional image guidance such as perfusion can be considered at the segmentation step [30].

Deep learning networks have significantly advanced super-resolution algorithms in medical imaging, thanks to the vast number of archived structural images available for training these models [31], [32]. However, progress in applying deep learning to ^{13}C HP imaging has been hindered by the limited dataset. As of the end of 2022, only 143 brain-related and 84 cardiac ^{13}C HP imaging studies had been conducted globally [33]. This scarcity of data presents a major challenge for training deep learning models in this area. Integrating deep learning techniques with the 3D PBSR reconstruction method would yield further improvements in enhancing HP images in the future.

V. CONCLUSION

In this study, the feasibility of enhancing spatial resolution using the proposed volumetric PBSR method was demonstrated in phantoms and *in vivo* cardiac metabolic images. Since structurally non-identified tissue regions are not restored regardless of the patch size, precise segmentation of tissue compartments is required for optimal performance.

Supplementary Material

Refer to Web version on PubMed Central for supplementary material.

Acknowledgments

This work was supported in part by the National Institute of Health under Grant R01NS107409, Grant R01HL170039, Grant P30DK127984, Grant P41EB015908, Grant S10OD018468, and Grant S10RR029119; in

part by the Muscular Dystrophy Association under Grant MDA963281, and in part by U.S. Army Medical Research Acquisition Activity under Grant W81XWH2210485.

Biographies

SUNG-HAN LIN was born in Taichung, Taiwan, in 1984. He received the B.S. and M.S. degrees in entomology from Taiwan University, in 2008, and the Ph.D. degree in medical imaging and radiological sciences from Chang Gung University, Taiwan, in 2021.

After completing the Ph.D. degree, he embarked on a postdoctoral research fellowship with the University of Texas Southwestern Medical Center, Dallas, TX, USA, where he continued his research in medical imaging. His scholarly contributions include a book chapter and over 15 journal articles in the field of MRI. He holds two patents. His research interests include the development of novel MR pulse sequences and image processing algorithm, metabolic imaging using hyperpolarized ^{13}C MRI, and their clinical translation.

Dr. Lin was a recipient of the 27th International Conference on Magnetic Resonance in Biological Systems Young Investigator Award, in 2016. He is a Review Editor of the *Frontiers in Neurology*.

JUNJIE MA received the B.S. degree in applied chemistry from Beihang University, Beijing, China, in 2016, and the Ph.D. degree in biomedical engineering from the University of Texas Southwestern Medical Center, Dallas, TX, USA, in 2021.

He has been with GE Healthcare, since 2021, as a Cardiac MR Scientist. He is the author of eight journal research articles and more than 20 conference abstracts. His research interest includes fast imaging methods for cardiac MR.

Dr. Ma was a recipient of Magna Cum Laude Awards (ISMRM), in 2019 and 2021, and the China National Scholarship, in 2013 and 2014.

JAE MO PARK (Member, IEEE) received the B.S. degree in electrical engineering from Yonsei University, Seoul, South Korea, in 2005, and the M.S. and Ph.D. degrees in electrical engineering from Stanford University, Stanford, CA, USA, in 2009 and 2012, respectively.

Before attending the graduate school, he was a Manager with SK Telecom, Seoul, between 2005 and 2007. He completed his postdoctoral training with the Stanford University School of Medicine, Stanford, CA, USA. He moved to the University of Texas Southwestern Medical Center, Dallas, TX, USA in 2016 as an Assistant Professor and has been Associate Professor since 2022 when he received his tenure.

Prof. Park was named a Junior Fellow (ISMRM), in 2014, and is a member of the International Society of Magnetic Resonance in Medicine, the American Heart Association, the National Neurotrauma Society, and the Institute of Electrical and Electronics Engineers.

REFERENCES

[1]. Cunningham CH, Lau JYC, Chen AP, Geraghty BJ, Perks WJ, Roifman I, Wright GA, and Connelly KA, “Hyperpolarized ^{13}C metabolic MRI of the human heart: Initial experience,” Circulat. Res, vol. 119, no. 11, pp. 1177–1182, 2016. [PubMed: 27635086]

[2]. Rider OJ, Apps A, Miller JJJJ, Lau JYC, Lewis AJM, Peterzan MA, Dodd MS, Lau AZ, Trumper C, Gallagher FA, Grist JT, Brindle KM, Neubauer S, and Tyler DJ, “Noninvasive in vivo assessment of cardiac metabolism in the healthy and diabetic human heart using hyperpolarized ^{13}C MRI,” Circulat. Res, vol. 126, no. 6, pp. 725–736, Mar. 2020. [PubMed: 32078413]

[3]. Apps A, Lau JYC, Miller JJJJ, Tyler A, Young LAJ, Lewis AJM, Barnes G, Trumper C, Neubauer S, Rider OJ, and Tyler DJ, “Proof-of-principle demonstration of direct metabolic imaging following myocardial infarction using hyperpolarized ^{13}C CMR,” JACC, Cardiovascular Imag, vol. 14, no. 6, pp. 1285–1288, Jun. 2021.

[4]. Park JM, Reed GD, Liticker J, Putnam WC, Chandra A, Yaros K, Afzal A, MacNamara J, Raza J, Hall RG, and Baxter J, “Effect of doxorubicin on myocardial bicarbonate production from pyruvate dehydrogenase in women with breast cancer,” Circulat. Res, vol. 104, no. 50, pp. 1568–1570, 2020.

[5]. Lau AZ, Chen AP, Ghugre NR, Ramanan V, Lam WW, Connelly KA, Wright GA, and Cunningham CH, “Rapid multislice imaging of hyperpolarized ^{13}C pyruvate and bicarbonate in the heart,” Magn. Reson. Med, vol. 64, no. 5, pp. 1323–1331, Nov. 2010. [PubMed: 20574989]

[6]. Tyler A, Lau JYC, Ball V, Timm KN, Zhou T, Tyler DJ, and Miller JJ, “A 3D hybrid-shot spiral sequence for hyperpolarized imaging,” Magn. Reson. Med, vol. 85, no. 2, pp. 790–801, Feb. 2021. [PubMed: 32894618]

[7]. Ma J, Chen J, Reed GD, Hackett EP, Harrison CE, Ratnakar J, Schulte RF, Zaha VG, Malloy CR, and Park JM, “Cardiac measurement of hyperpolarized ^{13}C metabolites using metabolite-selective multi-echo spiral imaging,” Magn. Reson. Med, vol. 86, no. 3, pp. 1494–1504, Sep. 2021. [PubMed: 33821504]

[8]. Reed GD, Ma J, Park JM, Schulte RF, Harrison CE, Chen AP, Pena S, Baxter J, Derner K, Tai M, Raza J, Liticker J, Hall RG, Sherry AD, Zaha VG, and Malloy CR, “Characterization and compensation of inhomogeneity artifact in spiral hyperpolarized^{13}C imaging of the human heart,” Magn. Reson. Med, vol. 86, no. 1, pp. 157–166, Jul. 2021. [PubMed: 33547689]

[9]. Ma J, Malloy CR, Pena S, Harrison CE, Ratnakar J, Zaha VG, and Park JM, “Dual-phase imaging of cardiac metabolism using hyperpolarized pyruvate,” Magn. Reson. Med, vol. 87, no. 1, pp. 302–311, Jan. 2022. [PubMed: 34617626]

[10]. Dwork N, Gordon JW, Tang S, O’Connor D, Hansen ESS, Laustsen C, and Larson PEZ, “Di-chromatic interpolation of magnetic resonance metabolic images,” Magn. Reson. Mater. Phys., Biol. Med, vol. 34, no. 1, pp. 57–72, Feb. 2021.

[11]. Farkash G, Markovic S, Novakovic M, and Frydman L, “Enhanced hyperpolarized chemical shift imaging based on a priori segmented information,” Magn. Reson. Med, vol. 81, no. 5, pp. 3080–3093, May 2019. [PubMed: 30652358]

[12]. Ehrhardt MJ, Gallagher FA, McLean MA, and Schönlieb C, “Enhancing the spatial resolution of hyperpolarized carbon-13 MRI of human brain metabolism using structure guidance,” Magn. Reson. Med, vol. 87, no. 3, pp. 1301–1312, Mar. 2022. [PubMed: 34687088]

[13]. Ma J and Park JM, “Super-resolution hyperpolarized ^{13}C imaging of human brain using patch-based algorithm,” Tomography, vol. 6, no. 4, pp. 343–355, Dec. 2020. [PubMed: 33364424]

[14]. Coupé P, Manjón JV, Chamberland M, Descoteaux M, and Hiba B, “Collaborative patch-based super-resolution for diffusion-weighted images,” NeuroImage, vol. 83, pp. 245–261, Dec. 2013. [PubMed: 23791914]

[15]. Kaul S, Glasheen W, Ruddy TD, Pandian NG, Weyman AE, and Okada RD, “The importance of defining left ventricular area at risk in vivo during acute myocardial infarction: An experimental evaluation with myocardial contrast two-dimensional echocardiography,” Circulation, vol. 75, no. 6, pp. 1249–1260, Jun. 1987. [PubMed: 3032476]

[16]. Wang Z, Bovik AC, Sheikh HR, and Simoncelli EP, “Image quality assessment: From error visibility to structural similarity,” IEEE Trans. Image Process, vol. 13, no. 4, pp. 600–612, Apr. 2004. [PubMed: 15376593]

[17]. Denney TS, “Bayesian image reconstruction from Fourier-domain samples using prior edge information,” J. Electron. Imag, vol. 14, no. 4, Oct. 2005, Art. no. 043009.

[18]. Haldar JP, Hernando D, Song S, and Liang Z, “Anatomically constrained reconstruction from noisy data,” Magn. Reson. Med, vol. 59, no. 4, pp. 810–818, Apr. 2008. [PubMed: 18383297]

[19]. Knoll F, Holler M, Koesters T, Otazo R, Bredies K, and Sodickson DK, “Joint MR-PET reconstruction using a multi-channel image regularizer,” IEEE Trans. Med. Imag, vol. 36, no. 1, pp. 1–16, Jan. 2017.

[20]. Rink K, Benkhedah N, Berger MC, Gnahm C, Behl NGR, Lommen JM, Stahl V, Bachert P, Ladd ME, and Nagel AM, “Iterative reconstruction of radially-sampled 31P bSSFP data using prior information from 1 H MRI,” Magn. Reson. Imag, vol. 37, pp. 147–158, Apr. 2017.

[21]. Obert AJ, Gutberlet M, Kern AL, Kaireit TF, Grimm R, Wacker F, and Vogel-Claussen J, “^{1}H-guided reconstruction of ^{19}F gas MRI in COPD patients,” Magn. Reson. Med, vol. 84, no. 3, pp. 1336–1346, 2020. [PubMed: 32060989]

[22]. Buades A, Coll B, and Morel J-M, “A non-local algorithm for image denoising,” in Proc. IEEE Comput. Soc. Conf. Comput. Vis. Pattern Recognit. (CVPR), vol. 2, Jun. 2005, pp. 60–65.

[23]. Rousseau F, “Brain hallucination,” in Computer Vision—ECCV (Lecture Notes in Computer Science), vol. 5302, Forsyth D, Torr P, and Zisserman A, Eds. Berlin, Germany: Springer, 2008, doi: 10.1007/978-3-540-88682-2_38.

[24]. Zhao Y, Wang R, Jia W, Yang J, Wang W, and Gao W, “Local patch encoding-based method for single image super-resolution,” Inf. Sci, vols. 433–434, pp. 292–305, Apr. 2018.

[25]. Schroeder MA, Lau AZ, Chen AP, Gu Y, Nagendran J, Barry J, Hu X, Dyck JRB, Tyler DJ, Clarke K, Connelly KA, Wright GA, and Cunningham CH, “Hyperpolarized ^{13}C magnetic resonance reveals early- and late-onset changes to in vivo pyruvate metabolism in the failing heart,” Eur. J. Heart Failure, vol. 15, no. 2, pp. 130–140, Feb. 2013.

[26]. Dodd MS, Atherton HJ, Carr CA, Stuckey DJ, West JA, Griffin JL, Radda GK, Clarke K, Heather LC, and Tyler DJ, “Impaired in vivo mitochondrial krebs cycle activity after myocardial infarction assessed using hyperpolarized magnetic resonance spectroscopy,” Circulat., Cardiovascular Imag, vol. 7, no. 6, pp. 895–904, Nov. 2014.

[27]. Lewis AJM, Miller JJ, Lau AZ, Curtis MK, Rider OJ, Choudhury RP, Neubauer S, Cunningham CH, Carr CA, and Tyler DJ, “Noninvasive immunometabolic cardiac inflammation imaging using hyperpolarized magnetic resonance,” Circulat. Res, vol. 122, no. 8, pp. 1084–1093, Apr. 2018. [PubMed: 29440071]

[28]. Lewis AJM, Tyler DJ, and Rider O, “Clinical cardiovascular applications of hyperpolarized magnetic resonance,” Cardiovascular Drugs Therapy, vol. 34, no. 2, pp. 231–240, Apr. 2020. [PubMed: 32020468]

[29]. Lin S, Harrison CE, Derner K, Erfani Z, and Park JM, "Identification of cardiac phase in hyperpolarized ^{13}C cardiac MRI using multiphase 1H MRI and unitized 3D patch-based reconstruction," in Proc. Int. Soc. Magn. Reson. Med, 2024, p. 4569.

[30]. Bøgh N, Olin RB, Hansen ES, Gordon JW, Bech SK, Bertelsen LB, Sánchez-Heredia JD, Blicher JU, Østergaard L, Ardenkjær-Larsen JH, Bok RA, Vigneron DB, and Laustsen C, ''Metabolic MRI with hyperpolarized [1–^{13}C]pyruvate separates benign oligemia from infarcting penumbra in porcine stroke," J. Cerebral Blood Flow Metabolism, vol. 41, no. 11, pp. 2916–2927, Nov. 2021.

[31]. Dang Q-V and Lee G-S, "Document image binarization with stroke boundary feature guided network," IEEE Access, vol. 9, pp. 36924–36936, 2021.

[32]. Wang B, Lian Y, Xiong X, Zhou H, Liu Z, and Zhou X, "DCT-net: Dual-domain cross-fusion transformer network for MRI reconstruction," Magn. Reson. Imag, vol. 107, pp. 69–79, Apr. 2024.

[33]. (2023). Hyperpolarized Pyruvate (^{13}C) Injection. Investigator's Brochure. National Cancer Institute. [Online]. Available: http://imaging.cancer.gov

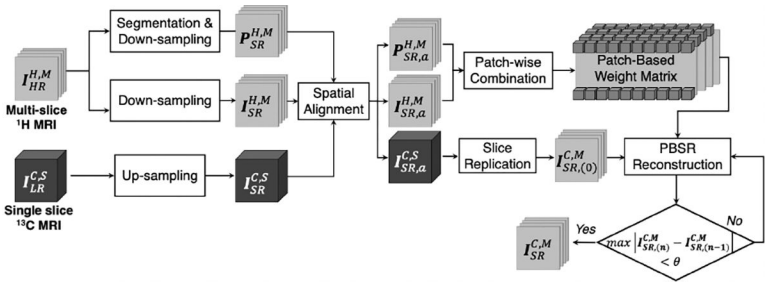

FIGURE 1.

Schematic view of the volumetric PBSR reconstruction process. Multi-slice high-resolution ^{1}H images ($I_{HR}^{H,M}$) are down-sampled and segmented to a targeted super-resolution ($I_{SR}^{H,M}$) and segmented to create probability maps ($P_{SR}^{H,M}$). In parallel, single-slice low-resolution ^{13}C metabolite maps ($I_{LR}^{C,M}$) are up-sampled to the target resolution ($I_{SR}^{C,S}$) and spatial aligned with the processed ^{1}H images and probability maps ($I_{SR,a}^{H,M}$, $P_{SR,a}^{H,M}$), which are used to calculate a patch-based weight matrix (PBWM) with a designated patch. Finally, multiple-slice super-resolution ^{13}C images ($I_{SR}^{C,M}$) are reconstructed initially from replicating the aligned ^{13}C image ($I_{SR,a}^{C,S}$) to a multi-slice volume, then by iteratively applying the PBWM until the maximum error between iterations becomes below a predetermined threshold (θ).

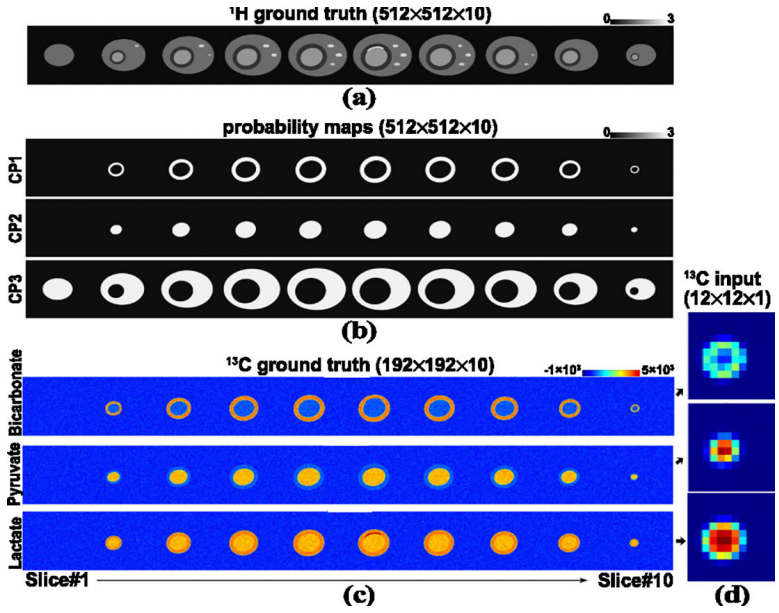

FIGURE 2.

A volumetric $^{1}H/^{13}C$ digital phantom for simulating the PBSR reconstruction. (a) High-resolution anatomical images for ^{1}H MRI (matrix size = 512 × 512 × 10). (b) Probability maps generated from the ^{1}H images for compartments: myocardium (CP1), ventricle (CP2), and the rest tissue region (CP3). (c) The ground truth metabolic images in a targeted resolution (192 × 192 × 10) for [^{13}C]bicarbonate, [1-^{13}C]pyruvate and [1-^{13}C]lactate. (d) Low-resolution ^{13}C maps used as input images (12 × 12 × 1).

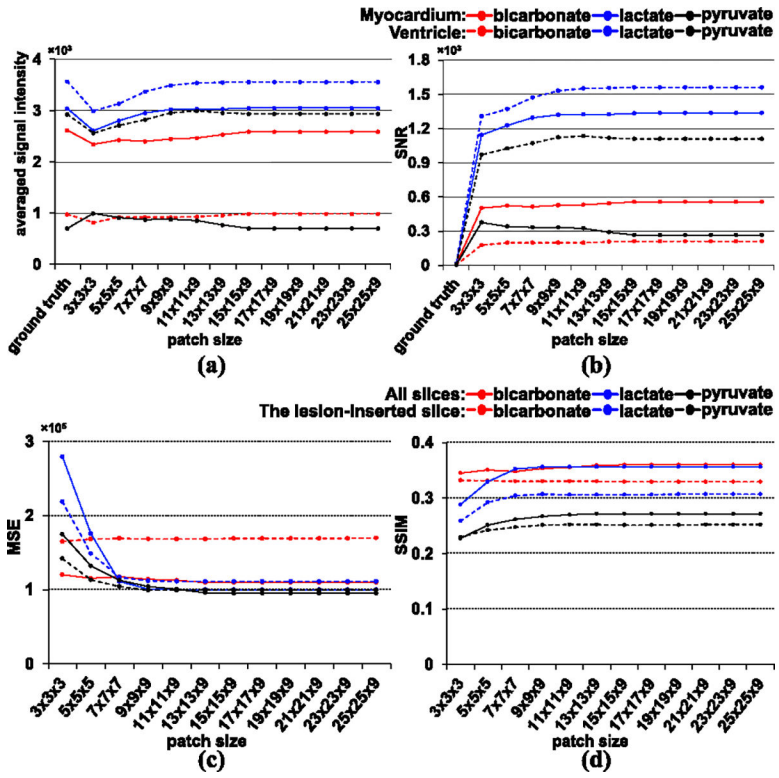

FIGURE 3.

Performance of the PBSR reconstruction with varying patch sizes. [^{13}C]Bicarbonate (red lines), [1-^{13}C]lactate (blue), and [1-^{13}C]pyruvate (black) of the simulated metabolic digital phantom were reconstructed using the volumetric PBSR method with various sizes of patches. (a) Averaged signal intensity and (b) SNR were measured from the myocardium (solid lines) and the ventricle (dashed lines). For each patch size, (c) mean square error (MSE) and (d) structural similarity index measure (SSIM) between the reconstructed images and the ground truth were calculated from the entire volume (all 10 slices, solid lines) and the lesion-containing slice only (6th slice; dashed lines).

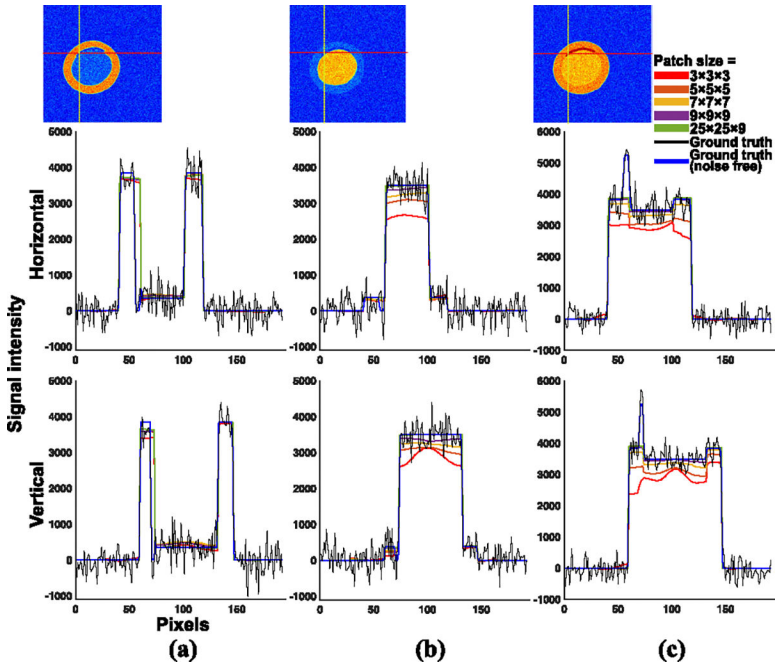

FIGURE 4.

Cross-sectional signal intensity over the ischemic lesion in the digital phantom. Cross-sectional signal intensity profiles for the lesion-inserted slice (6^{th} slice) in reconstructed metabolites as well as the ground truth are shown for (a) [^{13}C]bicarbonate, (b) [1-^{13}C]pyruvate, and (c) [1-^{13}C]lactate along the horizontal (top panel) and the vertical (bottom panel) reference lines with selected patch sizes, including the smallest four patches (3 × 3 × 3, 5 × 5 × 5, 7 × 7 × 7, 9 × 9 × 9), the largest patch (25 × 25 × 9), and the ground truth (with and without noise).

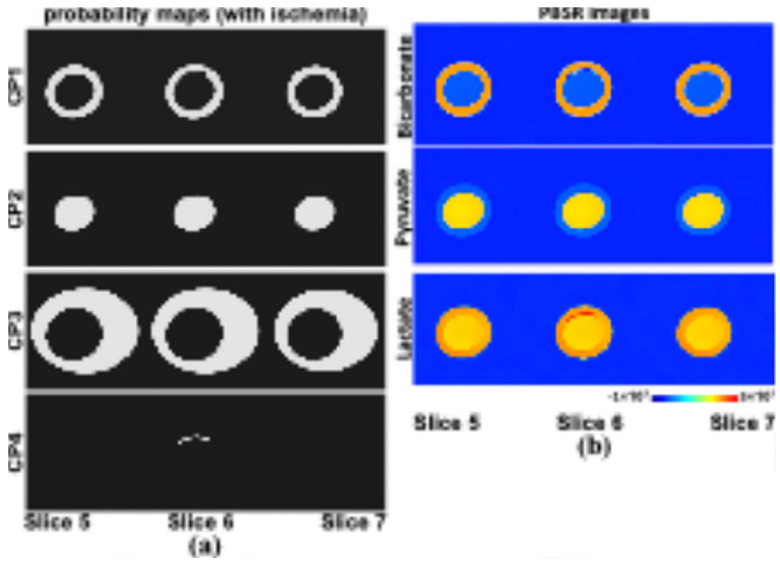

FIGURE 5.

PBSR-reconstructed ^{13}C images with additional ^{1}H probability map for the ischemic lesion. (a) A separate probability map for the ischemic lesion (CP4) in addition to those for myocardium (CP1), ventricle (CP2), and the rest tissue (CP3) was applied. (b) The PBSR-reconstructed images for [^{13}C]bicarbonate, [1-^{13}C]pyruvate, and [1-^{13}C]lactate. Only the lesion-bearing slice (6^{th}) and its adjacent slices (5^{th} and 7^{th}) are shown.

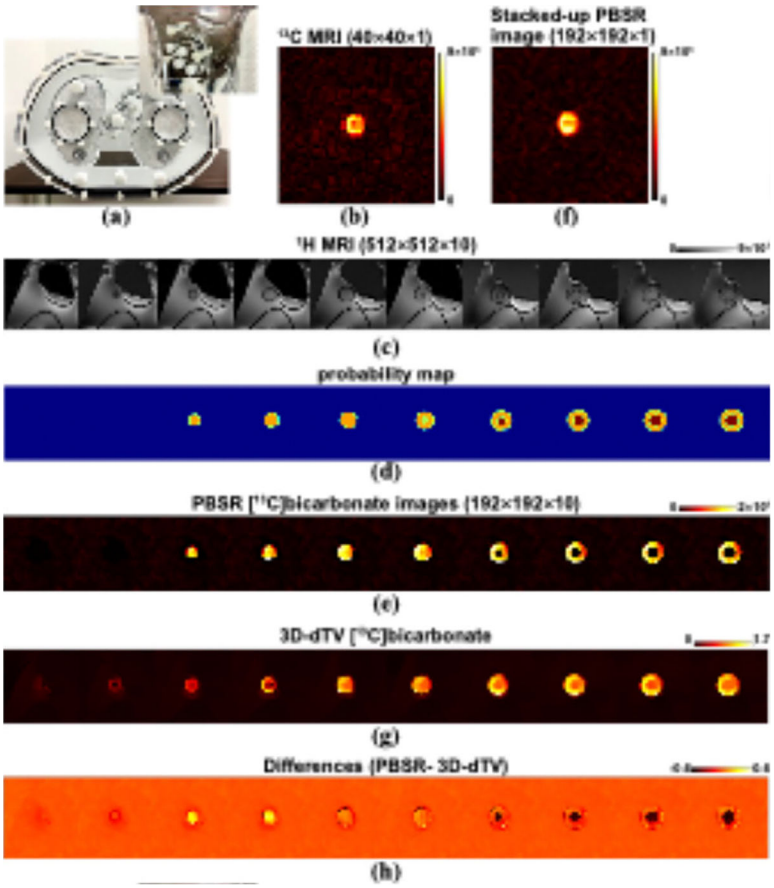

FIGURE 6.

Multi-slice reconstruction of a torso phantom using the PBSR. The PBSR algorithm was applied to an anthropomorphic torso phantom with a [^{13}C]bicarbonate-filled heart insertion (a). (b) The single-slice low-resolution input image (matrix size = 40 × 40× 1) were reconstructed with guidance from (c) the structural high-resolution images (matrix size = 512 × 512× 10) and the (d) corresponding segmented probability maps to (e) multi-slice super-resolution images (matrix size = 192 × 192× 10) in the targeted matrix size. The signal intensities were maintained after the PBSR reconstruction as shown in (f) the projected bicarbonate map along the slice direction (matrix size = 192 × 192× 1). (g) [^{13}C]Bicarbonate image, reconstructed by the 3D-dTV, showed signal bleeding from the myocardium into the neighboring compartment that doesn't contain any ^{13}C signal. (h) Differences between the PBSR-reconstructed images and the 3D-dTV-reconstructed images. The probability maps were illustrated with four compartments: ventricle (dark red), myocardium (orange), plastic walls of the phantom (light green), and the rest (blue). (c-e) and (g-h) present the central region only (256 × 256× 10 in ^{1}H and 20 × 20× 1 in ^{13}C) for display purpose.

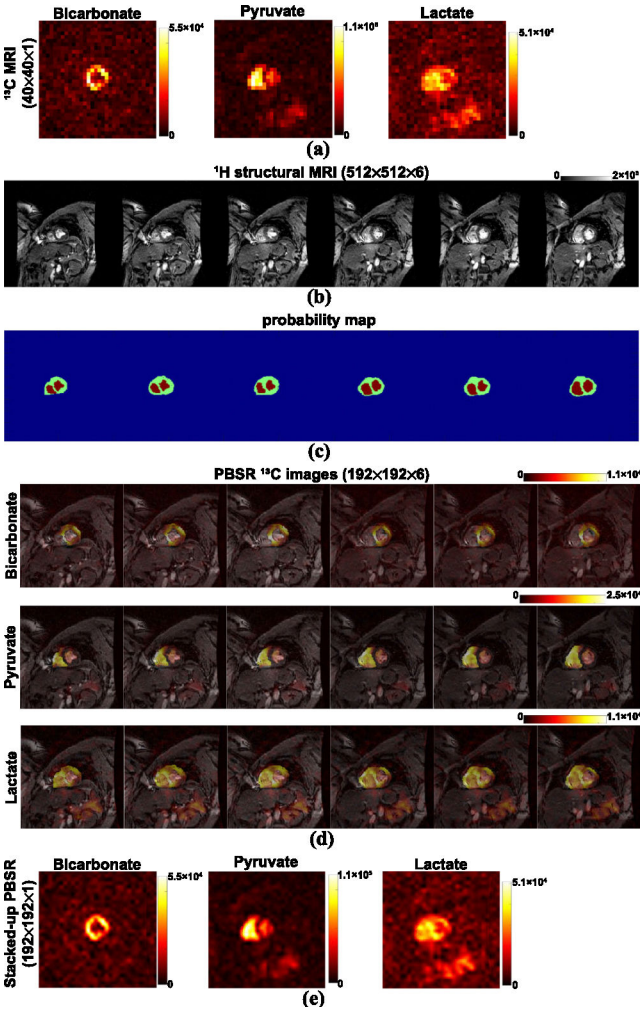

FIGURE 7.

In vivo cardiac images of HP ^{13}C metabolites reconstructed by volumetric PBSR (short-axis plane). The PBSR reconstruction method was applied to metabolite images of (a) HP [^{13}C]bicarbonate, [1-^{13}C]pyruvate, and [1-^{13}C]lactate acquired from a healthy human subject. From (b) ^{1}H structural images (matrix size = 512 × 512× 10), (c) probability maps for three compartments were obtained: ventricle (dark red), myocardium (light green), and the rest (blue). The acquired single-slice low-resolution HP ^{13}C images (matrix size = 40 × 40× 1) were reconstructed to (d) six-slice high-resolution images (matrix size = 192 × 192× 6). The reconstructed ^{13}C images are overlaid to the corresponding anatomical images. (e) The signal intensities of the stacked-up reconstructed images were comparable to those of the input images.

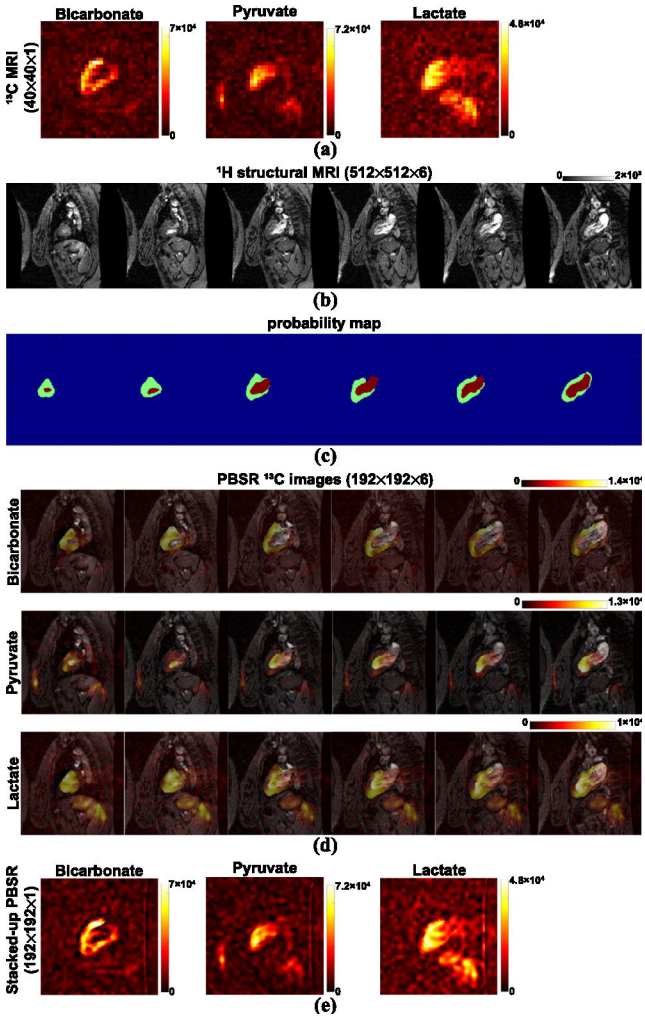

FIGURE 8.

In vivo cardiac images of HP ^{13}C metabolites reconstructed by volumetric PBSR (long-axis plane). The PBSR reconstruction method was applied to metabolite images of (a) HP [^{13}C]bicarbonate, [1-^{13}C]pyruvate, and [1-^{13}C]lactate acquired from the same subject. From (b) ^{1}H structural images (matrix size = 512 × 512× 10), (c) probability maps for three compartments were obtained: ventricle (dark red), myocardium (light green), and the rest (blue). The acquired single-slice low-resolution HP ^{13}C images (matrix size = 40 × 40× 1) were reconstructed to (d) six-slice high-resolution images (matrix size = 192 × 192× 6). The reconstructed ^{13}C images are overlaid to the corresponding anatomical images. (e) The signal intensities of the stacked-up reconstructed images were comparable to those of the input images.

TABLE 1.

The entropy of the input images.

	Digital Phantom	**Torso Phantom**	***In Vivo***
[^{13}C]bicarbonate	3.4807	4.9305	5.4514
[l-^{13}C]pyruvate	2.7105	N.A.	5.5960
[l-^{13}C]lactate	2.9746	N.A.	6.2334

TABLE 2.

Structural similarity index measure (SSIM) between original and PBSR-reconstructed *IN VIVO* ^{13}c images.

image plane	[^{13}C]bicarbonate	[l-^{13}C]pyruvate	[l-^{13}C]lactate
short-axis	0.9764	0.9758	0.9750
long-axis	0.9740	0.9746	0.9741